water

Article

Confining Stress Response to Hydraulic Fracturing Volumetric Opening on the Representative Volume Element (RVE) Scale

Shuaifang Guo [1], Yunxing Cao [1,2], Li Wang [3,*], Xinsheng Zhang [3,*], Wenying Zhang [3], Haixiao Lin [3], Zhengzheng Cao [3] and Bingbing Meng [1]

[1] School of Resources & Environment, Henan Polytechnic University, Jiaozuo 454000, China; gshuaifang@163.com (S.G.); yxcao17@126.com (Y.C.); meng123bingb@163.com (B.M.)
[2] Gas Geology and Engineering Research Center, Henan Polytechnic University, Jiaozuo 454000, China
[3] International Joint Research Laboratory of Henan Province for Underground Space Development and Disaster Prevention, School of Civil Engineering, Henan Polytechnic University, Jiaozuo 454003, China; zhangwy1230@163.com (W.Z.); hpulhx@hpu.edu.cn (H.L.); caozz@hpu.edu.cn (Z.C.)
* Correspondence: wlcjwh@163.com (L.W.); zhangxswei@163.com (X.Z.)

Abstract: Confining stress response is considered an accompanying behavior of hydraulic fracturing. Along these lines, an evaluation model of confining stress response was presented in this work. It was established on a rock representative volume element (RVE) and based on the hydraulic volumetric opening model, which stems from the theories of poroelasticity, breakdown damage, and hydraulic fracture mechanics. From the extracted outcomes, it was demonstrated that the confinement of the stress response depends on the matching among the characteristic parameters $(\varepsilon_b, \varepsilon_s, m)$ of the rock breakdown, the volumetric opening, and channel flow regimes of the fracturing fluid. Examples in four limiting fracturing regimes show that (1) the confinement of the stress response is strongly determined by the existence of various fracturing regimes and takes place in a different manner during fracture initiation and opening. More specifically, during fracturing initiation, the ratio of the confining stress response to the far-field stress $(Pcmax/\sigma_h)$ is 2.0500 in the M regime, 1.9600 in the $\widetilde{M}$ regime, 2.7126 in the K regime, and 1.7448 in the $\widetilde{K}$ regime, while when the fracture is opened, these values (P_C/σ_h) are 1.8994, 1.8314, 1.6378, and 1.2846, respectively. (2) The impact of the confined stress response to the fluid pressure is also affected by the fracturing regimes; e.g., in both M and $\widetilde{M}$ regimes, the peak confinement stress responses lag behind peak pore pressures, but in the K and $\widetilde{K}$ regimes, lag off disappears. (3) The pore volumetric opening (V_p^e) leads to an increase in the confining stress response, while the fracture opening (V_p^{d}) leads to a reduction in the confining stress response.

Keywords: hydraulic fracture; poroelasticity; damage; confining stress; fracturing propagation regime

check for updates

Citation: Guo, S.; Cao, Y.; Wang, L.; Zhang, X.; Zhang, W.; Lin, H.; Cao, Z.; Meng, B. Confining Stress Response to Hydraulic Fracturing Volumetric Opening on the Representative Volume Element (RVE) Scale. *Water* **2023**, *15*, 4184. https://doi.org/10.3390/w15234184

Academic Editor: Vittorio Di Federico

Received: 30 October 2023
Revised: 23 November 2023
Accepted: 30 November 2023
Published: 4 December 2023

1. Introduction

Hydraulic fracturing (HF) is considered a vital method for advancing petroleum, whether in conventional or unconventional natural gas [1–3]. A surplus of fluid is expelled, surpassing what poroelasticity can withstand, aiming to stimulate hydraulic volumetric openings in reservoir formations. Consequently, permeability is enhanced [4–6]. However, in return, this volumetric opening will stimulate the manifestation of an additional confining stress on the material skeleton, which is called the confining stress response [7–9]. Since micro- or nano-pores in the skeleton matrix are the main sorption space for unconventional gas, confining stress response will inevitably reduce the matrix permeability and hamper gas production [10–12]. Therefore, it is necessary to evaluate the confining stress response during the implementation of an HF.

The confining stress response due to HF treatment was first noted by Cleary [13]. This effect was called far-field confining stress and described as back stress, namely σ_b, which was different from confining stress. The author also reported that back stress arises from the alteration of the pore pressure due to fluid infiltration into the surrounding rocks.

Since Detournay and Cheng [14] associated back stress with Biot's theory of poroelasticity, various types of poroelastic effects have been reported in the literature.

On top of that, Detournay and Cheng [15] included poroelastic effects in the PKN model by setting up a constitutive relationship between the fluid pressure and width of fracture with the poroelastic coefficient. Kovalyshen [16] associated poroelastic effects with a radial model by establishing a boundary integral form of back stress.

On another front, studies on the poroelastic effects based on the application of direct numeric methods can be classified into two branches, namely, single-fracture models and multiple-fracture models.

In the first branch, Boone and Ingraffea [17] studied the poroelastic effect by carrying out Finite Element Method (FEM) simulations and demonstrated that the back stress was the minimum at the borehole and maximum at the fracture tip. In another interesting work, Golovin and Baykin [18] demonstrated the influence of Biot's number on pore pressure and fracture width distributions. Gao and Detournay [19] investigated two fracture regimes in laboratory hydraulic fracturing and concluded that poroelasticity can significantly affect the magnitude of the injection pressure. Baykin [20] proved that the diffusion scale plays a central role in the poroelastic effects, while Donstsov [21] developed an efficient computation method of poroelastic stress, which is a combination of the one-dimensional Carter leak-off model and back stress. Moreover, Sarris and Papanastasiou [22–24] studied the poroelasto-plastic effects and showed that a rabbit-ear-shaped plastic zone was developed near the fracture tip, and demonstrated that the poroelasto-plastic effect was responsible for larger net pressure and fracture width.

In another branch, multiple fracturing modeling was performed to demonstrate stress shadow and fracturing interference based on the utilization of various numeric methods, like the PFC model [25], XFEM [26,27], Abaqus model [28], DNF model [29,30], phase field model [31], UDEC [10], the lattice model [32], etc. Particularly, Dontsov and Suarez-Rivera [33] found that the propagation of multiple closely spaced hydraulic fractures varies dramatically with respect to the fracture propagation regimes.

To sum up, previous studies on the poroelastic effect have mainly focused on the global fracture scale, whereas the conclusions are significantly dependent on the fracture geometry and other engineering factors. However, from the HF evaluation perspective, it is necessary to establish a stress disturbance evaluation model, namely, a representative volume element (RVE) evaluation model. The RVE model can integrate the macro attributes of the reservoir and injected fluid, such as elasticity, toughness, leakage, permeability, flow rate, viscosity, and compressibility, and then, the coupling and matching relationship between the reservoir cohesive fracture characteristics and fracture propagation mechanism can be characterized.

In this work, an RVE evaluation model of confining stress response was established based on the hydraulic volumetric opening (HVO) model. The HVO model, proposed by Wang et al. [34], is a combination of the poroelasticity, breakdown damage, and hydraulic fracture mechanics theories. The pore volumetric opening and fracture volumetric opening were unified in an RVE by matching the behaviors of the channel flow in a KGD fracture, the porous elastic opening, and the cohesive breakdown. Based on the HVO model, the confining stress response model was established by utilizing the deformation compatibility during the hydraulic fracturing opening. Finally, as an example, under the four limiting hydraulic fracturing regimes, the evolution law of stress disturbance was exhibited based on the HVO model.

2. The Model of Confining Stress Response to the HVO

2.1. Staged Expressions of the HVO

Considering an RVE in the hydraulic fracturing region, as is shown in Figure 1, the original state of the material was isotropic, homogeneous, perfectly elastic, and permeated with void spaces of various shapes and sizes, such as microcracks, fissures, and pores, all of which were idealized as pore volume. Since the fluid injection (represented by $q_{in} > q_{out}$)

and pore volume are saturated and the pore pressure is built up, this effect, in turn, leads to the pore volume being elastically opened, the matrix skeleton being elastically stretched and broken, and eventually, the formation of a trunk fracture from the chained skeletons' breakdown. According to the increase in the skeleton stress, this process can be segmented into three distinct stages, characterized by four typical states:

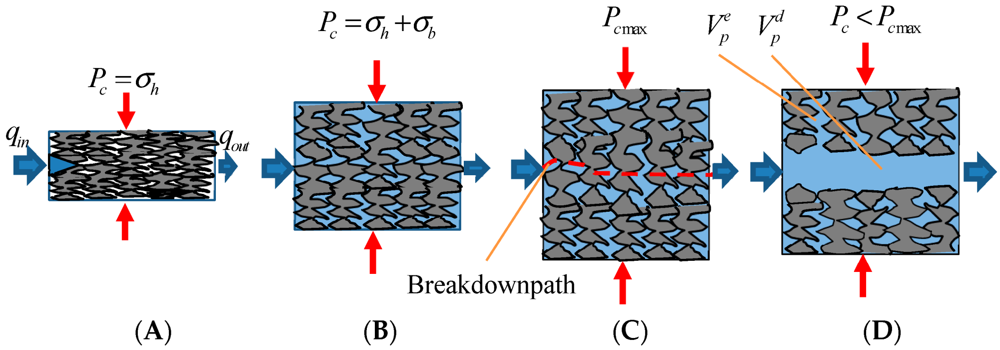

Figure 1. Hydraulic fracturing process in the RVE. The '**A**' is original compression state; '**B**' represents the stress neutralization state; '**C**' is the critical fracture state; '**D**' is the fracture opening-steady state.

Stage I, which can be described as the compression-relieving stage, involves the original compressive stress on the skeletons being gradually balanced to zero by the pore pressure. In Stage II, this stage can be described as an elastic stretching phase, during which the matrix skeleton undergoes stretching due to the opening of the pore volume. In Stage III, which is a cohesive breakdown stage, the chained cohesive breakdown occurs, the trunk fracture takes its form, and fracture opening occurs.

Correspondingly, the four typical states are the following: 'A' is the original compression state under the confining stress; 'B' represents the stress neutralization state, wherein the skeleton stress becomes zero as the pore pressure balances the confining stress. 'C' is the critical state, where the elastically stretching microcracking approaches the end and the macro-breakdown is about to happen, and 'D' is the fracture opening that approaches a steady state.

For this tip process, three hydraulic volumetric openings can be defined:

The pore volumetric opening, V_p^e, is defined as the volumetric opening of pores per unit bulk volume of rocks. In terms of quantity, it represents the increment in the elastic net volume of void spaces of various shapes and sizes due to the influence of pore fluid pressure. The fracture volumetric opening, V_p^d, is defined as the trunk fracture volumetric opening per unit bulk volume of the rocks. For a plane strain fracturing and cubic element of a unit bulk volume, $V_p^d = w$, where w is the fracture width. The hydraulic volumetric opening, V_p, is the total volumetric opening per unit bulk volume of rocks. Quantitatively, it signifies the net increment in porosity resulting from hydraulic fracturing. The progressive development of these volumetric openings can be described as follows:

$$V_p = \begin{cases} V_p^e, & \text{stages: I, II} \\ V_p^e + V_p^d, & \text{stage: III} \end{cases} \tag{1}$$

Applying the poroelasticity theory [35], incremental expressions for volumetric openings can be found in the literature [34], as follows

$$dV_p^e = C_m \left\{ (1 - \phi_0 - \tilde{\alpha}) dP_p + \left(\frac{1}{\tilde{\alpha}} - 1 \right) d\sigma' \right\} \tag{2a}$$

$$dV_p^d = C_m \left(\tilde{\alpha} P_p + \frac{1}{\tilde{\alpha}} \sigma' \right) \frac{-df(D)}{f(D)} \tag{2b}$$

where C_m is the flexibility of the matrix material; D is scalar damage representing the progress of the chained breakdown with $0 \le D \le 1$; $f(D)$ stands for an evolving function, representing the evolution of the bulk modulus, compressibilities, and Biot's coefficient due to cohesive breakdown; and $\widetilde{\alpha} = (1-\alpha_0)f(D)$ refers to the residual Biot coefficient relative to the original Biot coefficient α_0.

2.2. Breakdown Criterion and Evolving Laws of State Variables

The breakdown criterion is defined on a quasi-static evolving path of the skeleton stress, which is characterized by a smoothed peak and a long tail, shown by $A-B-C-D$ in Figure 2. The progress of cohesive breakdown can be represented by scalar damage as follows:

$$D = \begin{cases} 0, & \varepsilon_0 \le \varepsilon_I \le 0, \text{ stage: I} \\ \left(\frac{\varepsilon_I}{\varepsilon_s}\right)^m, & 0 < \varepsilon_I \le \varepsilon_b, \text{ stage: II} \\ 1-\left(\frac{(\Delta\sigma_{br})^2}{(\varepsilon_b-\varepsilon_I)k_b+\Delta\sigma_{br}}+\sigma_r\right)\frac{1}{E_0\varepsilon_I}, & \varepsilon_b < \varepsilon_I, \text{ stage: III} \end{cases} \tag{3}$$

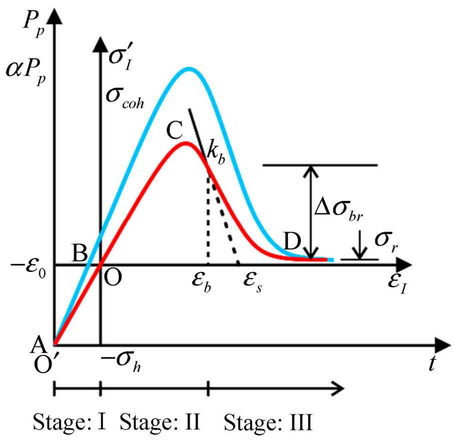

Figure 2. Quasi-static evolving path of the skeleton stress. The parameter σ_I' signifies the contrast between the effective stresses. σ_{coh} represents cohesive stress. P_p denotes pore pressure. αP_p represents the effective pore pressure, controlled by stretch bulk strain ε_I and fluid injection time t. The OCD curve represents a cohesive traction decomposition model [33]. The blue curve represents evolution law of $P_p - t$; The red curve represents evolution law of $\sigma_I' - \varepsilon_t$.

Of the parameters in Equation (3), ε_s signifies the ultimate strain anticipated for a flawless brittle fracture, ε_b indicates the transition strain from the evolution of microcracks to the propagation of macrocracks, m denotes the brittle index, σ_r represents residual stress, k_b is the ratio of the stress drop at ε_b reflecting the intensity of the stress drop, and $\Delta\sigma_{br}$ is the stress drop from the initiation of macrocrack propagation to the residual stress. All these parameters can be determined from the uniaxial tensile stress–strain curve, as illustrated in Figure 2.

Ensuring a mathematically smooth connection at ε_b requires the construction of the two parameters $\Delta\sigma_{br}$ and k_b from other measured parametric groups $(\varepsilon_b, \varepsilon_s, m)$, as follows:

$$\Delta\sigma_{br} = E_0\left[1-\left(\frac{\varepsilon_b}{\varepsilon_I}\right)^m\right]\varepsilon_b - \sigma_r \tag{4a}$$

$$k_b = \left[1-\left(\frac{\varepsilon_b}{\varepsilon_s}\right)^m(m+1)\right]E_0 \tag{4b}$$

Thus, it can be seen that the breakdown behavior is stipulated by the parametric group $(\varepsilon_b, \varepsilon_s, m)$ under anhydrous conditions, except for the basic Young modulus E_0.

The comparative advantage of the smoothed-peak stress curve over the sharp-peak models, such as the classic cohesive zone model [36] and the exponential softening model [22], is that the microcracking process prior to the large-scale breakdown can be reflected. Additionally, the advantage of the long tail is that a continuous function is used to represent the gradual fracture opening, which, in fact, prolongs the tip process to the whole of the fracture.

2.3. Model of Confining Stress Response on RVE

In order to establish the confining stress response model of the fluid injection around the fracture during the process of hydraulic fracturing, the RVE element of the reservoir was selected in the steady flow state during the fracturing process (Figure 3a), and the schematic diagram of its plane stress model (Figure 3b) was constructed. The total in situ confining stress is the sum of the back stress and the far-field stress, namely $P_c = \sigma_b + \sigma_h$.

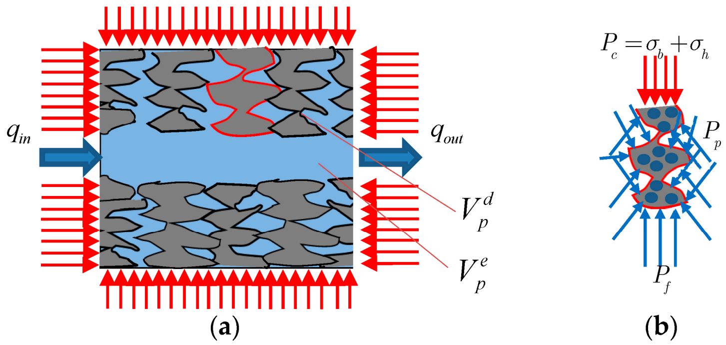

Figure 3. (**a**) The RVE element and (**b**) forces on a skeleton.

As can be observed from Figure 3b, the bulk volume expansion induced by the hydraulic volumetric opening is constrained by the combination of the pore pressure and additional confining stress. In the direction of the fracture opening, it was assumed that the pore pressure P_p and fracture pressure P_f are equal; thus, $P_p = P_c$. Therefore, combined with the principle of mechanical equilibrium and deformation compatibility, this constraint can be described by using the compatibility relation as follows:

$$\varepsilon_v(P_p) - \varepsilon_v(\sigma_b) = \varepsilon_v(V_p) \tag{5}$$

where $\varepsilon_v(P_p)$ is the bulk volume expansion due to pore pressure, $\varepsilon_v(\sigma_b)$ represents the bulk volume compression due to back stress, and $\varepsilon_v(V_p)$ denotes the total bulk volume expansion due to the hydraulic volumetric opening.

From Equation (2), dV_p can be rewritten into the following expression:

$$\begin{aligned} dV_p &= C_m\left\{\tilde{\alpha}P_p\frac{-df(D)}{f(D)} + (1-\phi_0-\tilde{\alpha})dP_p\right\} + C_m\left\{\frac{1}{\tilde{\alpha}}\sigma'_I\frac{-df(D)}{f(D)} + \left(\frac{1}{\tilde{\alpha}}-1\right)d\sigma'_I\right\} \\ &= \left[dV_p^d(P_p) + dV_p^e(dP_p)\right] + \left[dV_p^d(\sigma'_I) + dV_p^e(d\sigma'_I)\right] \\ &= dV_p(P_p) + dV_p(\sigma'_I) \end{aligned} \tag{6}$$

where $V_p(P_p)$ is the portion of the volumetric opening due to the pore pressure, and $V_p(\sigma'_I)$ represents that due to skeleton stress. In the same way, $\varepsilon_v(V_p)$ can be decomposed as follows:

$$\begin{aligned} \varepsilon_v(V_p) &= \frac{\Delta V_b(P_p)}{V_b} + \frac{\Delta V_b(\sigma'_I)}{V_b} \\ &= \frac{1}{V_b}\int\left[dV_b^d(P_p) + dV_b^e(dP_p)\right] + \frac{1}{V_b}\int\left[dV_b^d(\sigma'_I) + dV_b^e(d\sigma'_I)\right] \\ &= \varepsilon_v(P_p) + \varepsilon_v(\sigma'_I) \end{aligned} \tag{7}$$

where V_b is the unit bulk volume, $dV_b^d(P_p)$ is the incremental bulk volume due to the fracture volume opening merely attributed to pore pressure, and $dV_b^e(dP_p)$ stands for the incremental bulk volume due to the pore volume opening attributed to the incremental pore pressure. It is the same with $dV_b^d(\sigma')$ and $dV_b^e(d\sigma')$.

The substitution of Equation (5) with Equation (7) yields the following expression:

$$\varepsilon_v(\sigma_b) = -\varepsilon_v(\sigma_I') = -\int\left[\frac{dV_b^d(\sigma_I')}{V_b} + \frac{dV_b^e(d\sigma_I')}{V_b}\right] \tag{8}$$

where $dV_b^d(\sigma')$ represents the rigid expansion to be replaced by the fracture volumetric opening $dV_p^d(\sigma_I')$; $dV_b^e(d\sigma_I')$ signifies the poroelastic expansion to be translated by the ratio C_{bc}/C_{pc} of compressibilities, which was defined by Zimmerman. Thus, it can be described as follows:

$$\varepsilon_v(\sigma_b) = -\int\left[\frac{dV_p^d(\sigma_I')}{V_b} + \frac{C_{bc}}{C_{pc}}\frac{dV_p^e(d\sigma_I')}{V_p}\right] \tag{9}$$

By including the terms in Equation (7), and letting $V_b = 1$ and $V_p = \phi_0 V_b$ (not that V_p is the initial pore volume in V_b here), the following equation can be derived:

$$\varepsilon_v(\sigma_b) = -C_m\int\left[-\frac{1}{\widetilde{\alpha}}\sigma_I'\frac{df(D)}{f(D)} + \frac{C_{bc}}{\phi_0 C_{pc}}\left(\frac{1}{\widetilde{\alpha}} - 1\right)d\sigma_I'\right] \tag{10}$$

The relations between those compressibilities were used by Zimmerman, and = the initial compression under confining stress $\varepsilon_{v0} = -\sigma_h/K_b$ was superposed as follows:

$$\varepsilon_v(P_c) = \int\frac{C_m}{\widetilde{\alpha}}\left[\sigma_I'\frac{df(D)}{f(D)} - d\sigma_I'\right] - \frac{\sigma_h}{K_b} \tag{11}$$

By using the elasticity law $\varepsilon_v(P_c) = P_c/K_b$, the total confining stress can be obtained as follows:

$$P_c = \int\left[\sigma_I'\frac{df(D)}{f(D)} - d\sigma_I'\right] - \sigma_h \tag{12}$$

By assuming $f(D) = (1-D)^{\frac{1}{n}}$, the bulk volume expansion and confining stress are as follows:

$$\varepsilon_v(P_c) = \int\frac{C_m}{\widetilde{\alpha}}\left[\frac{\sigma_I'}{n}\frac{dD}{(1-D)} - d\sigma_I'\right] - \frac{\sigma_h}{K_b} \tag{13}$$

$$P_c = \int\left[\frac{\sigma_I'}{n}\frac{dD}{(1-D)} - d\sigma_I'\right] - \sigma_h \tag{14}$$

This is the constitutive relationship between the total in situ confining stress response and the hydraulic fracturing volumetric opening. The integration was executed along the injection time t or the skeleton strain ε_I, while it was demonstrated that the confining stress response was determined not only by the rock elasticity properties but also by the characteristics of cohesive breakdown and fracturing propagation regimes, which were represented by the parametric group $\{n, m, \varepsilon_b, \varepsilon_s\}$.

3. Incorporating the Regimes of Hydraulic Fracturing Propagation

Various works in the literature [37–40] have proposed hydraulic fracturing regimes based on simple planar models, including KGD, PKN, and radial, based on the controlling equations in hydraulic fracturing. It was found that the interactions of channel flow in a planar fracture with rock elasticity, toughness, and leak-off can be categorized into four distinct limiting fracturing regimes and intermediate fracturing regimes within the parameter space that is expanded by the dimensionless viscosity C_m and dimensionless toughness K_m. Moreover, the various fracturing regimes take on varying temporal evolutions of the fracture width, length, and fluid pressure distribution.

The incorporation of fracturing regimes into the HVO model was employed to combine the channel flow of the fracturing regimes with the cohesive breakdown and volumetric opening, to obtain the proper evolution of the HVO model. From another point of view, Carter's leak-off, addressing fluid loss from the planar fracture, governs the fracturing regimes, while Darcy's law, which governs the volumetric openings of the pores, concerns the porous flow of the filtrated fluid. Therefore, this incorporation is indeed a unification of Carter's leak-off model and Darcy's law in the HVO model.

In fact, this incorporation can be realized by matching the temporal evolution of the fracture volumetric opening $V_p^d(t)$ with the temporal evolution of a KGD fracture width $w(x,t)$ to obtain the proper evaluation of the parameter group $\{\varepsilon_b, \varepsilon_s, m, n\}$. In this operation, the KGD fracture width, denoted as $w(x,t)$, represents the fluid load in the HVO model, and the parameter group refers to the constitutive response of the cohesive breakdown and the volumetric opening of the rock.

It is well established that the fracturing regimes provide fracture width distribution $w(x,t)$ along the fracture length, as is shown in Figure 4. The problem lies with the selection of the position x. More specifically, because the HVO model plays the role of a constitutive relationship, it should be endowed with all the characteristics of the cohesive breakdown and volumetric opening for the entire hydraulic fracturing process. Obviously, only at the fracture inlet (where $x = 0$), the fracture width $w(0,t)$ can satisfy this requirement, while at other positions (like $x = \xi$), the width evolution will undergo the same as that at the fracture inlet. However, the experience is incomplete because of the propagation delay.

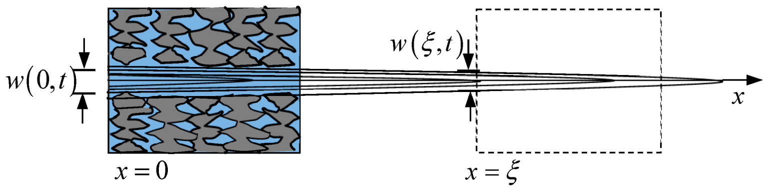

Figure 4. Matching between the RVE fracture opening and a KGD fracture opening.

Since the analytical solutions for fracture width $w(0,t)$ can be found in the article [40], the properly evaluated parameter group $\{\varepsilon_b, \varepsilon_s, m, n\}$ can be obtained by carrying out curve fitting between $V_p^d(t)$ and $w(0,t)$.

4. Examples

Examples were used to demonstrate how to evaluate the confining stress response due to HF and the constitutive relationship between the confining stress response and HVOs in four limiting fracturing cases. These four limiting cases corresponded to the four limiting fracturing regimes; these, include the viscosity–storage-dominated regime M, the viscosity–leak-off-dominated regimes $\widetilde{M}$, the toughness–storage regime K, and the toughness–leak-off-dominated regime $\widetilde{K}$, respectively.

4.1. The Process for Obtaining the Parameters of the Confining Stress Response Model

The procedure followed the following sequences: parameter measurement; parameter transition; determination of the computation time; obtaining the best-fitted parameter group via curve fitting; and obtaining the evolving hydraulic volumetric opening and confining stress response.

4.1.1. Parameter Measurement

The evaluation of the confining stress response and the volumetric opening was based on the poromechanical parameters that were collected from the field. In the examples, the basic parameters for all the fracturing cases were taken from a coal bed methane (CBM) reservoir formation located in Qinshui Basin in Shanxi Province, China; a reservoir formation thickness of $h = 6$ m, Young's modulus of $E_0 = 12.7$ GPa, Poisson's ratio of $v = 0.3$, injection flow rate of $Q_m = 6\ \mathrm{m}^3/\mathrm{min}$, viscosity of $\mu = 0.001$ Pa $\cdot$ s, and fluid compressibility of $C_f = 0$ were assumed. The other parameters related to the fracturing regimes, such as tensile strength σ_t, static confining stress σ_0, original confining stress σ_h, permeability k, porosity ϕ_0, and Biot's coefficient α_0, are listed in Table 1.

Table 1. Measured parameters in four limiting cases.

Fracturing Cases	σ_t/MPa	σ_0/MPa	σ_h/MPa	k_0/mD	ϕ/%	α_0	Regimes
1	0.36	7.3	5.8	0.01	2	0.6	M
2	0.36	7.3	5.8	1000	10	0.6	$\widetilde{M}$
3	28.00	7.3	5.8	0.01	2	0.6	K
4	28.00	7.3	5.8	200	10	0.6	$\widetilde{K}$

4.1.2. Parameter Conversion

Because the fracturing regimes were derived from the KGD models, the measured parameters in Table 2 needed to be converted into the KGD system according to the relations shown in Table 2. In these conversions, r_0 is the size of micro-defects in rocks, and c represents the diffusion coefficient. Based on these, the KGD parameters for fracturing regime recognition were calculated and are shown in Table 3.

Table 2. Conversions from the basic parameters into the KGD system.

Basic Parameters	Conversion	Parameters for KGD Model
σ_t	$K_{IC} = \sigma_t\sqrt{2\pi r_0} \approx 0.12\sigma_t$	$K' = 4\left(\frac{2}{\pi}\right)^{1/2} K_{Ic}$
E, v	—	$E' = \frac{E}{1-v^2}; v' = 12v$
$k_0,\sigma_0,\alpha,\phi,\mu,C_{pp},C_f$	$k = k_0 e^{-(\sigma_0-\alpha P_p)}$ $c = \frac{k}{\phi\mu(C_{pp}+C_f)}$ $C_l \approx \frac{k\sigma_0}{\mu\sqrt{\pi c}}$	$C' = 2C_l$
Q_m, h, N	—	$Q_0 = Q_m/Nh$

Table 3. Parameters for the fracture regime recognition.

Fracturing Cases	E'/Gpa^{-1}	K'/MPa·m$^{1/2}$	μ'/Pa·s	C'/m·s$^{-1/2}$	K_m	C_m or C_k
M	14.25	0.13787	0.012	4.5931×10^{-6}	0.075	C_m: 0.1
$\widetilde{M}$	14.25	0.13787	0.012	1.9×10^{-3}	0.050	C_m: 4
K	14.25	10.724	0.012	4.5931×10^{-6}	5.800	C_k: 0.0542
$\widetilde{K}$	14.25	10.724	0.012	8.5653×10^{-4}	3.880	C_k: 1.421

4.1.3. Computation Time

Hu and Garagash [40] demonstrated that various fracturing regimes can be reduced to four distinct limiting and intermediate regimes in the dimensionless parametric space (K_m, C_m) or (K_m, C_k) through the following divisions:

$$\begin{array}{lll} M-\text{regime}: 0 < K_m < 1.2 & \& & 0 < C_m < 0.1; \\ \widetilde{M}-\text{regime}: 0 < K_m < 1.2 & \& & 4 < C_m; \\ K-\text{regime}: 3.8 < K_m & \& & 0 < C_k < 0.542; \\ \widetilde{K}-\text{regime}: 3.8 < K_m & \& & 1.421 < C_k; \end{array} \quad (15)$$

where K_m represents the dimensionless toughness coefficient, C_m stands for the dimensionless leak-off coefficient in viscosity-dominated regimes, and C_k indicates the dimensionless leak-off coefficient in toughness-dominated regimes. These coefficients are defined as follows:

$$\begin{array}{l} K_m = \frac{K'}{E'}\left(\frac{E'}{\mu' Q_0}\right)^{\frac{1}{4}} \\ C_m = \left(\frac{t}{t_*}\right)^{\frac{1}{6}} = \left(\frac{E' C'^6 t}{\mu' Q_0^3}\right)^{\frac{1}{6}} \\ C_k = K_m^{-\frac{2}{3}} C_m \end{array} \quad (16)$$

where t represents the injection time, and $t_* = \mu' Q_0^3 / E' C'^6$ is a characteristic time.

From these divisions, it can be argued that if these limiting fracturing regimes hold, the computation time t in the different regimes can be determined as follows:

$$\begin{array}{l} t_M < 0.1^6 \frac{\mu' Q_0^3}{E' C'^6} \text{ for } M-\text{regime} \ ; \ t_K < 0.0542^6 \times 3.8^4 \frac{\mu' Q_0^3}{E' C'^6} \text{ for } K-\text{regime} \ ; \\ t_{\widetilde{M}} > 4^6 \frac{\mu' Q_0^3}{E' C'^6} \text{ for } \widetilde{M}-\text{regime} \ ; \ t_{\widetilde{K}} > 1.421^6 \times 3.8^4 \frac{\mu' Q_0^3}{E' C'^6} \text{ for } \widetilde{K}-\text{regime} \ ; \end{array} \tag{17}$$

According to these conditions, the computation times in the different regimes were determined and are listed in Table 2. The dimensionless coefficients for regime recognition are listed in Table 4.

Table 4. Identified evolving indices and rock damage parameters within the four limiting regimes.

Fracturing Cases	n	m	$\varepsilon_b/\varepsilon_{t0}$	$\varepsilon_s/\varepsilon_b$	k_b/E_0	σ_{ht}/σ_t	N
M	1.36	2.90	1.80	1.22	−1.179	0.97	40
$\widetilde{M}$	2.31	2.80	1.10	1.61	1.940×10^{-5}	0.82	10
K	3.65	1.00	0.38	2.00	0	0.19	50
$\widetilde{K}$	2.62	1.00	0.08	2.00	0	0.04	10

4.1.4. Curve Fitting

The curve fitting between $V_p^d(t)$ and $w(0,t)$ was carried out to obtain the best-fitted parameter group $\{n, m, \varepsilon_b, \varepsilon_s\}$ by adjusting the combination. The expressions for $w(0,t)$ in the four limiting regimes were drawn from [40], as follows:

$$w(0,t) = \begin{cases} 1.126\left(\frac{\mu'}{E't}\right)^{1/3}\left(\frac{E'Q_0^3}{\mu'}\right)^{1/6} t^{2/3}, & M-\text{regime} \\ 0.8165\left(\frac{C'^2\mu'}{E'Q_0 t}\right)^{1/4} \frac{Q_0}{C'} t^{1/2}, & \widetilde{M}-\text{regime} \\ 0.6828\left(\frac{K'^4}{E'^4 Q_0 t}\right)^{1/3}\left(\frac{E'Q_0}{K'}\right)^{2/3} t^{2/3}, & K-\text{regime} \\ 0.3989\left(\frac{K'^4 C'^2}{E'^4 Q_0^2 t}\right)^{1/4} \frac{Q_0}{C'} t^{1/2}, & \widetilde{K}-\text{regime} \end{cases} \tag{18}$$

The curve-fitting process followed the steps:

(1) The injection time, t, was given to calculate the skeleton strain as follows:

$$\varepsilon_I = -\frac{\sigma_h}{E_0} + \frac{t}{t_p}\varepsilon_t \tag{19}$$

where ε_t is the limiting tensile strain corresponding to tensile strength σ_t, $\varepsilon_t = \sigma_t / E_0$; t_p is a characterized time corresponding to ε_t and can be determined through a static tensile test. However, in this work, the value of $t_p = 1$ s was selected.

(2) D, $f(D)$, P_p and σ_I' were calculated.

(3) dV_p^e, dV_p^d, and dV_p, as well as V_p^e, V_p^d, and V_p, were calculated by accumulating $V_p^{e(n)} = V_p^{e(n-1)} + dV_p^{e(n)}$, etc.

(4) $V_p^d(t)$ was fitted with $w(0,t)$ to obtain the group with the best combination of parameters $\{n, m, \varepsilon_b, \varepsilon_s\}$ and the number of hydraulic fractures N.

(5) The change laws of V_p^e, V_p^d, V_p and P_c were obtained.

4.2. Physical Meanings of the Curve Fitting

Parametric groups $\{n, m, \varepsilon_b, \varepsilon_s\}$ in four limiting regimes were obtained through curve fitting and are listed in Table 4, upon which all the variables were obtained, including hydraulic volumetric openings, confining stress response, skeleton stress, pore pressure, and breakdown damage. In addition, both fracture number N and hydraulically tensile strength σ_{ht} were also obtained.

The curve fitting led to the fracture number $N > 1$ and hydraulic tensile strength being less than in the anhydrous conditions, $\sigma_{ht} < \sigma_t$. This reflects the physical meanings of the curve fitting.

The meaning for $N > 1$ is that, in the condition of a single fracture, $Q_m = Q_0$ will lead to a relatively large $w(0,t)$, meaning that the fracture volumetric opening $V_p^d(t)$ cannot match up. Only when $N > 1$, so that $Q_m = Q_0/hN$ and it generates a proper $w(0,t)$, can $V_p^d(t)$ match up well. This effect implies that, for a single KGD fracture, $w(0,t)$ is derived merely from the channel flow regimes without considering the constraints of the rock breakdown characteristics and overstates the fracture opening capacity. As far as the spatial distribution of these N fractures is concerned, it may be parallel or branching, while all fractures followed the distribution of the pre-existing crack. In the current mechanism, the two storage-dominated regimes M and K were recognized to be liable for the generation of more multiple fractures than the leak-off-dominated regimes $\widetilde{M}$ and $\widetilde{K}$.

The underlying reason for the hydraulic tensile strength σ_{ht} being less than the anhydrous tensile strength σ_t is that, in the hydraulic fracturing model, the fluid goes ahead of the fracture tip both in stages I and II, and microcracking before breakdown is permitted, which induces a more liable breakdown than in the anhydrous conditions. In the current fracturing mechanisms, it was found that σ_{ht}/σ_t in the toughness-dominated regimes K and $\widetilde{K}$ was significantly lower than that in the viscosity-dominated regimes M and $\widetilde{M}$, and that in the leak-off-dominated regimes $\widetilde{M}$ and $\widetilde{K}$ was less than in the storage-dominated regimes M and K.

All these effects reflect the physical meanings of the curve fittings, where, in an HF process, fluid injection is an active force represented by the fracture propagation regimes $w(0,t)$. Moreover, $V_p^d(t)$ is an adaption response, which is represented by the parameter group $\{n, m, \varepsilon_b, \varepsilon_s\}$, and the matching between them generates a number of fractures N and hydraulic tensile strength σ_{ht}.

4.3. Results and Validation

4.3.1. Hydraulic Volumetric Openings

The change patterns of hydraulic volumetric openings are depicted in Figure 5. The V_p^e first increased linearly from the compression state to a peak, followed by a decline to a low level as soon as the breakdown began. Then, V_p^d was increased following a power law. As a sum, V_p first increased following the pore volumetric opening, then reached a constant level as soon as the fracture volumetric opening occurred.

The hydraulic volumetric openings per single fracture in the multi-fracturing system at the end of the injection time t_s are listed in Table 5, and the total hydraulic volumetric openings for the multi-fracturing system are listed in Table 6. It was shown that the hydraulic volumetric openings in the high-toughness conditions (K and $\widetilde{K}$) were larger than those in the low-toughness conditions (M and $\widetilde{M}$), and those in the high-leak-off conditions ($\widetilde{M}$ and $\widetilde{K}$) were smaller than those in the low-leak-off conditions (M and K).

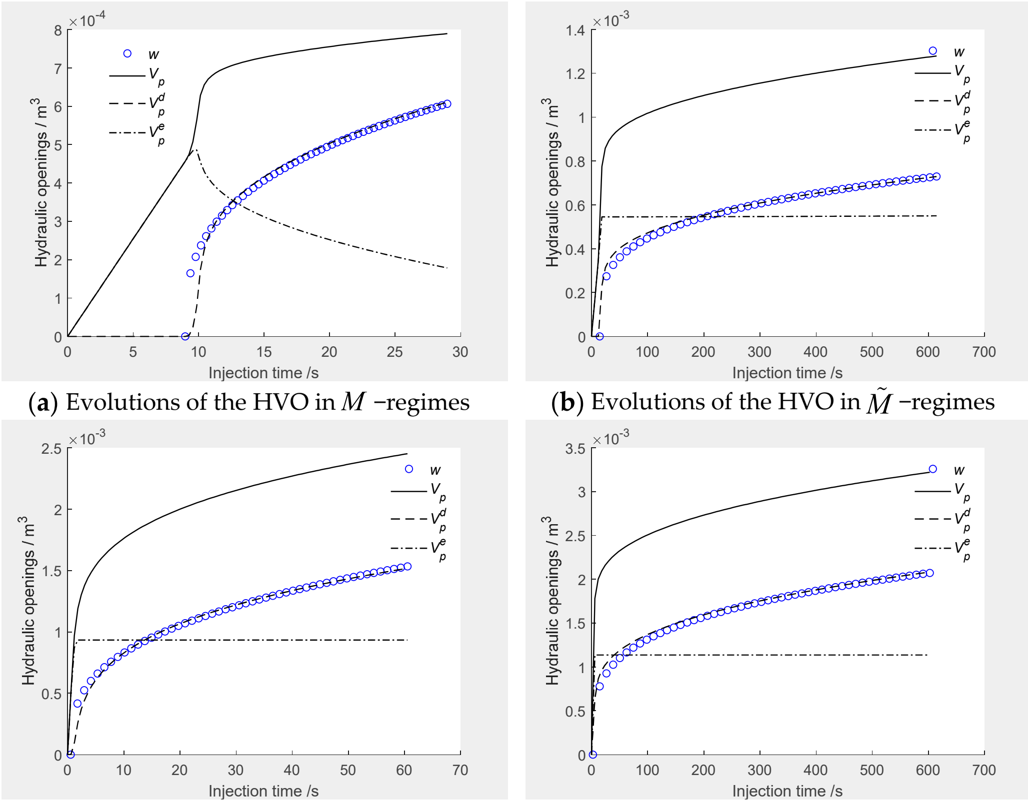

(**a**) Evolutions of the HVO in M −regimes (**b**) Evolutions of the HVO in $\tilde{M}$ −regimes

(**c**) Evolutions of the HVO in K−regimes (**d**) Evolutions of the HVO in $\tilde{K}$ −regimes

Figure 5. Evolutions of the hydraulic volumetric openings in the four limiting regimes.

Table 5. Hydraulic volumetric openings for a single fracture in the four limiting regimes.

Fracturing Cases	V_p^d $m^3 \times 10^{-4}$	V_p^e $m^3 \times 10^{-4}$	V_p $m^3 \times 10^{-4}$	V_p^d/ϕ_{ini} %	V_p^e/ϕ_{ini} %	V_p/ϕ_{ini} %
M	6.11	1.18	7.89	3.10	0.91	4.01
$\widetilde{M}$	7.29	5.50	13.00	0.73	0.55	1.28
K	16.00	9.34	25.00	7.87	4.74	12.61
$\widetilde{K}$	21.00	11.00	32.00	2.09	1.14	3.23

Table 6. Total hydraulic volumetric openings for the multi-fracturing system in four limiting regimes.

Fracturing Cases	V_p^d/m^3 $\times 10^{-3}$	V_p^e/m^3 $\times 10^{-3}$	V_p/m^3 $\times 10^{-3}$	V_p^d/ϕ_{ini} %	V_p^e/ϕ_{ini} %	V_p/ϕ_{ini} %
M	24.40	4.714	31.56	123.92	36.24	160.17
$\widetilde{M}$	7.29	5.499	13.00	7.30	5.50	12.80
K	80.00	46.60	125.00	393.39	236.94	630.34
$\widetilde{K}$	21.00	11.00	32.00	20.88	11.39	32.28

The changes in the skeleton stress (marked as effective stress) and pore pressure are shown in Figure 6, and the breakdown damage evolution is shown in Figure 7 (note that the negative strain represents the skeleton initially being under compression). From the comparisons between these plots, it is known that the change law of V_p^e inherits the evolution modes of the pore fluid pressure and effective stress, while the change in V_p^d inherits the evolution mode of the breakdown damage.

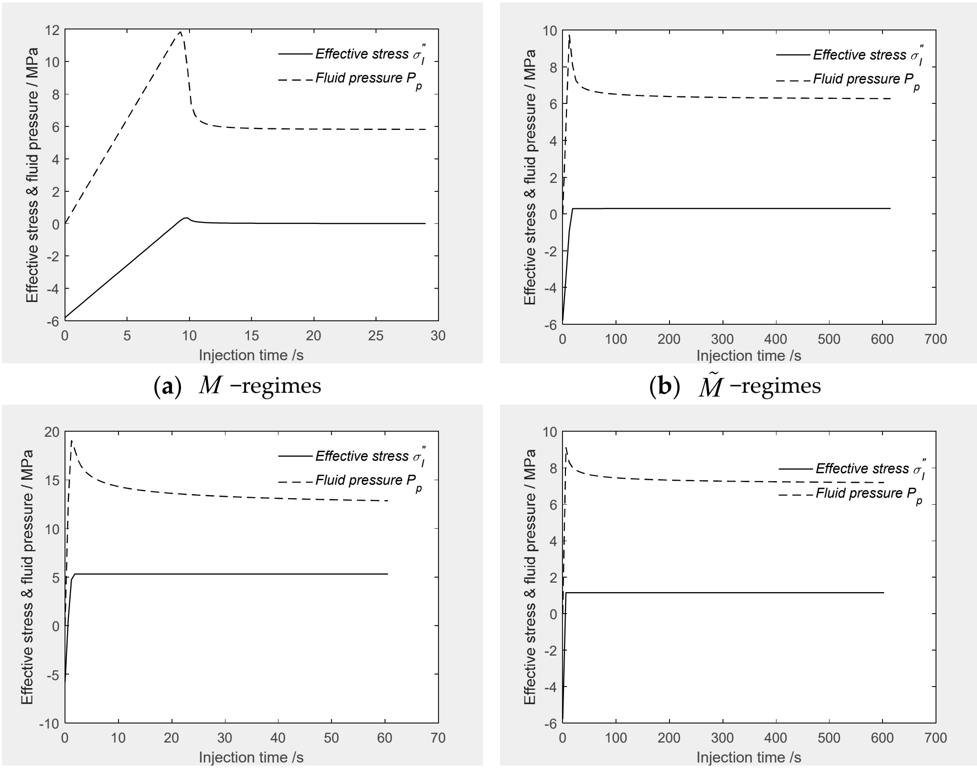

(**a**) M −regimes (**b**) $\tilde{M}$ −regimes

(**c**) K−regimes (**d**) $\tilde{K}$ −regimes

Figure 6. Evolutions of the effective stress values and fluid pressure in the four limiting regimes.

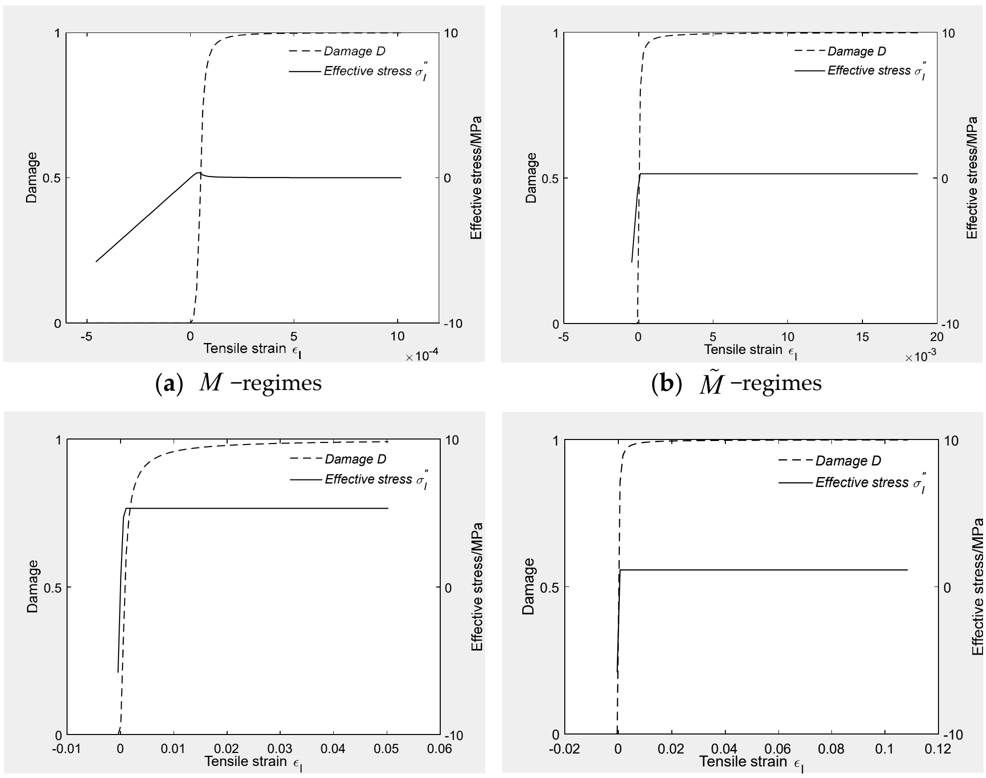

(**a**) M −regimes (**b**) $\tilde{M}$ −regimes

(**c**) K−regimes (**d**) $\tilde{K}$ −regimes

Figure 7. Contrast between the evolutions of the effective stress and damage via principal strain in four limiting regimes.

4.3.2. Confining Stress Response

The change in the confining stress $P_c(= \sigma_h + \sigma_b)$ with the fluid injection time in different fracturing regimes is shown in Figure 8. Generally, the confining stress P_c first exhibits an inverse law to the skeleton stress and fluid pressure since it was increased from the initial state $\sigma_h = -5.8$ MPa; it then rises to a compressive peak and then descends to a low level during compression as the fluid pressure and effective stress are removed.

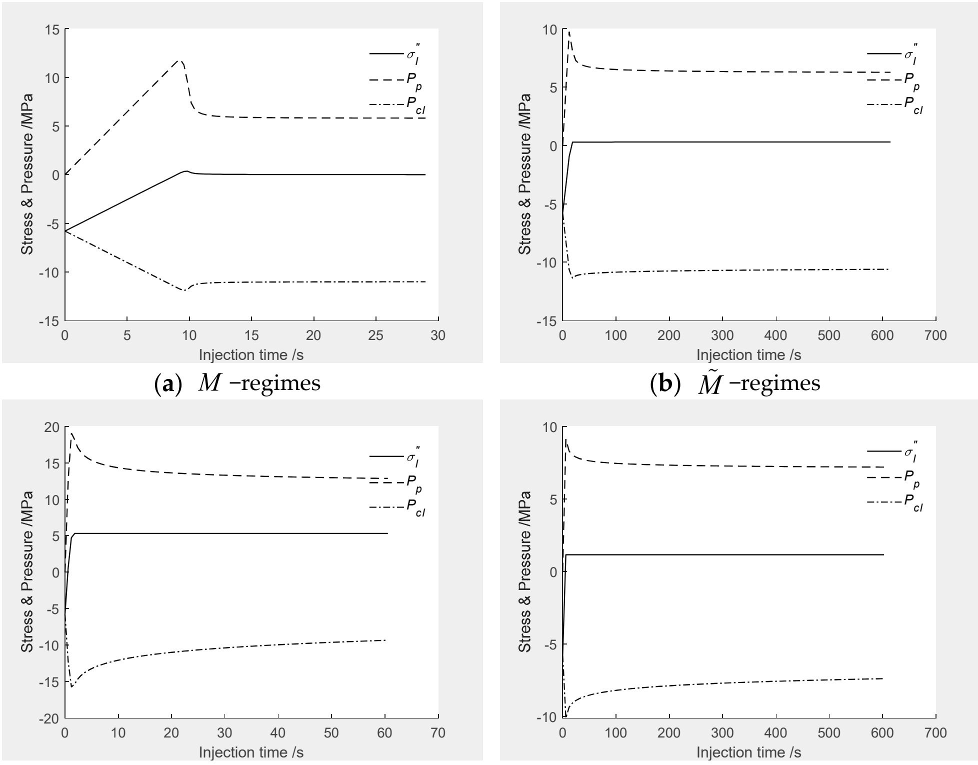

(**a**) M −regimes (**b**) $\tilde{M}$ −regimes

(**c**) ***K***−regimes (**d**) $\tilde{K}$ −regimes

Figure 8. Contrast between effective stress, fluid pressure, and confining stress.

From the description of the tip process shown in Figure 1, it is known that the time when the peak confining stress occurs corresponds to the region of the fracture tip where a breakdown is about to occur, and the long time span after the peak corresponds to the whole fracture body. Therefore, from Figure 8, the confinement of the stress distribution around a fracture can be speculated to be fracturing propagation, while the fracture tip is surrounded by a concentrated zone of the confining compressive stress, with the maximum $P_{c\max}$ in the center. Moreover, the fracture faces are surrounded by a less concentrated compressive zone on each side, with $P_c < P_{c\max}$. (Note that the sign conventions are the following: compressions ($P_{c\max}$, P_c, and σ_h) are negative and tensions ($P_{p\max}$, P_p, σ'_{Imax}, and σ'_{I}) are positive.)

The ratios of confining stress to the far-field confining stress, fluid pressure, and skeleton stress in the four limiting regimes are shown in Table 7, in which $P_{c\max}/\sigma_h$ and P_c/σ_h are the ratios of the maximum confining stress and steady confining stress after the peak to the far-field confining stress, respectively. From the two extracted ratios, the concentration of the confining stress at the fracture tip and the fracture body can be determined. From the recorded outcomes, the following can be argued: (1) the stress concentrations at the fracture tip are generally larger than in the fractured body for various fracturing regimes; (2) the concentrations in the storage-dominated regimes M and K are larger than in leak-off-dominated regimes $\widetilde{M}$ and $\widetilde{K}$ for both the fracture tip and body, which shows that the leak-off leads to a decrease in concentration.

Table 7. Ratios of confining stress to initial stress, skeleton stress, and fluid pressure.

Fracturing Regimes	$P_{c\max}/P_{p\max}$	P_c/P_p	$P_{c\max}/\sigma_h$	P_c/σ_h	$P_{c\max}/\sigma'_{\mathrm{I}max}$	P_c/σ'_{I}
M	−1.0059	−1.8932	2.0500	1.8994	−33.9551	−1672
$\widetilde{M}$	−1.1676	−1.6918	1.9600	1.8314	−38.3442	−35.8941
K	−0.8258	−0.7355	2.7126	1.6378	−2.9573	−1.7858
$\widetilde{K}$	−1.1099	−1.0349	1.7448	1.2846	−8.8151	−6.4904

4.3.3. Back Stress Effects

In Table 7, $P_{c\max}/P_{p\max}$ and P_c/P_p are the ratios of the confining stress to the pore pressure at the fracture tip and body, respectively, and represent the poroelastic effect where pore pressure generates confining stress. They show that at the fracture tip, $P_{c\max}/P_{p\max}$ approximates to the value of -1, and in the fractured body, P_c/P_p are 1.89 and 1.69 in the viscosity-dominated regimes and 0.73 and 1.03 in the toughness-dominated regimes. This effect indicates that at the fracture tip, confining stress is caused by the pore pressure and is slightly affected by the fracturing regimes. However, in the fractured body, confining stress is strongly affected by the fracturing regimes. In the viscosity-dominated regimes, the breakdown is completed; thus, confining that stress is mainly determined by the channel flow. Nevertheless, in the toughness-dominated regimes, the breakdown is incomplete; confining that stress response is hampered by incomplete cohesive tractions. The completeness of the breakdown is shown in Table 7, by $P_{c\max}/\sigma'_{\mathrm{I}\max}$ and P_c/σ'_{I}, where it is demonstrated that the skeleton stress σ'_I in the toughness-dominated regime is much larger than that in the viscosity-dominated regimes.

Furthermore, the back stress coefficient $\overline{\chi}$ can be calculated as follows [12]: $\overline{\chi} = \sigma_b/P_p = (P_c - \sigma_h)/P_p$, which is listed in Table 8. Clearly, it shows that back stress exhibits similar characteristics to confining stress.

Table 8. Back stress coefficient in the limiting fracturing regimes.

	M	$\widetilde{M}$	K	$\widetilde{K}$
$\overline{\chi}_{tip} = \sigma_{b\max}/P_{p\max}$	0.52	0.57	0.52	0.47
$\overline{\chi} = \sigma_b/P_p$	0.90	0.77	0.28	0.23

4.4. The Mechanisms of Confining Stress Response in the Four Limiting Regimes

The mechanisms of the confining stress response to the hydraulic volumetric opening can be observed in the plots of P_c vs. V_p in Figure 9 and the comparison of P_c vs. V_p, V_p^e, and V_p^d in various fracturing regimes in Figure 10.

Morphologically, these plots show similar characteristics to the constitutive relations of the stress vs. strain at anhydrous conditions, where the confining stress response and pore pressure initially increase to a peak, followed by a decrease to a low level as breakdown damage occurs. However, these constitutive responses are strongly governed by the hydraulic fracturing regimes.

One of these features is the peak shifting between the responses of confining stress and the pore pressure. In the viscosity-dominated regimes, the confining stress response lags behind the pore pressure, but in the toughness-dominated regimes, the peak shifting disappears. In addition, leak-off leads to more significant peak shifting in the $\widetilde{M}$ regime than in the M regime.

Another feature is that the time spans (measured according to the volumetric opening) of the confining stress responses vary with the various fracturing regimes. As can be ascertained from Figure 10a, in the viscosity-dominated regimes, the time spans are smaller than those in the toughness-dominated regimes.

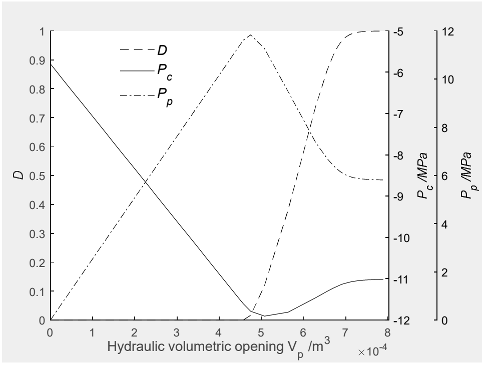

(**a**) M −regimes

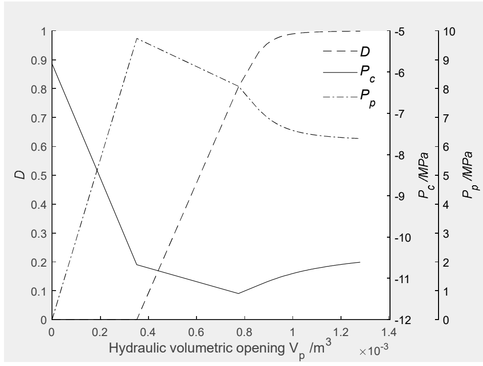

(**b**) $\tilde{M}$ −regimes

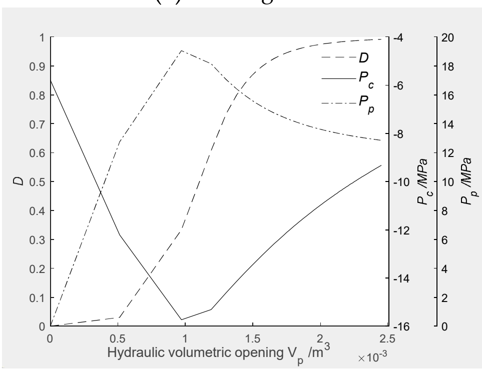

(**c**) ***K***−regimes

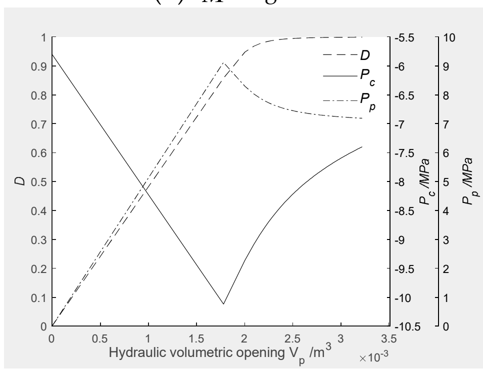

(**d**) $\tilde{K}$ −regimes

Figure 9. Contrast between evolutions of breakdown damage, confining stress, and fluid pressure via a hydraulic volumetric opening in four limiting regimes.

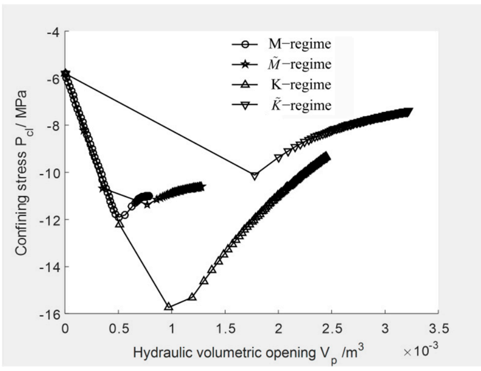

(**a**) Confining stress evolution via HVO in the four limiting regimes

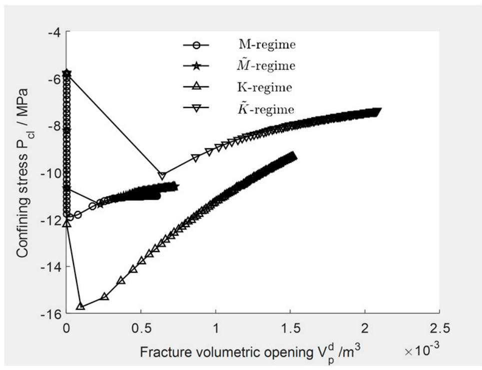

(**b**) Confining stress evolution via fracture volumetric opening in four limiting regimes

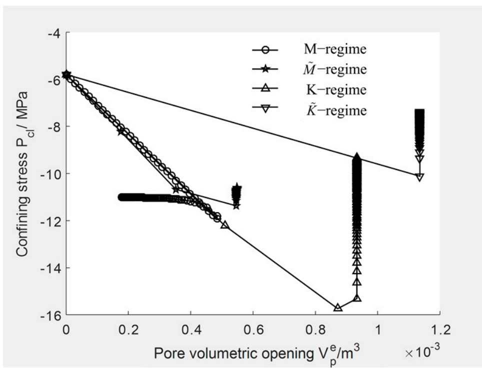

(**c**) Confining stress evolution via pore volumetric opening in four limiting regimes

Figure 10. Confining stress evolution via hydraulic volumetric openings.

The third is that the confining stress response time spans are governed by the synchronization of the evolutions of the pore volumetric opening and fracture volumetric opening.

As can be observed, fluid injection first leads to an increase in the pore pressure and, consequently, to the enhancement of the pore volumetric opening. In turn, confining stress response around the fracture is further stimulated, but as soon as breakdown happens, fracture opening leads to a pore pressure reduction, and, therefore, both the pore volumetric opening and confining stress are decreased.

In the M regime, the fracture is brittle, and a clear division line between the evolutions of the pore volumetric opening and fracture volumetric opening can be found, which means that as soon as breakdown begins, the pore volumetric opening stops at once. Therefore, a short peak confining stress response will happen, as is shown in Figure 11a. Nevertheless, in the $\widetilde{M}$, $K\&\widetilde{K}$ regimes, the evolving of the pore volumetric opening is blended with fracture opening at different degrees, which will lead to the manifestation of ductile fracture and long-peak confining stress responses, as is shown in Figure 11b–d.

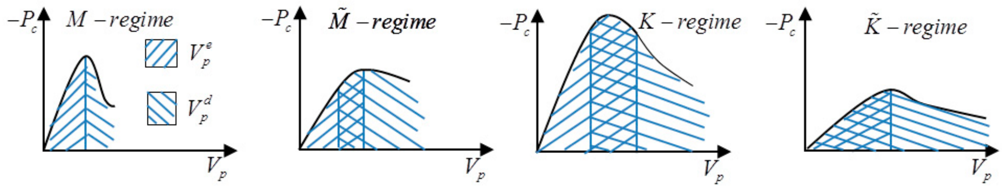

(**a**) M −regimes (**b**) $\tilde{M}$ −regimes (**c**) K−regimes (**d**) $\tilde{K}$ −regimes

Figure 11. Hydraulic fracturing mechanisms in four fracturing propagation regimes.

5. Conclusions

In this work, a theoretical framework of hydraulic volumetric opening (HVO) models was clarified, while the expression of the confining stress response was derived. Furthermore, the calculation of the hydraulic volumetric openings and confining stress response was clarified. By employing several examples, the change laws of the hydraulic volumetric openings and confining stress response, poroelastic effects, and constitutive relationships between the confining stress response and hydraulic volumetric openings were demonstrated.

(1) Confining stress concentrations P_c/σ_h at the fracture tip are generally larger than in the fractured body for varying fracturing regimes.

(2) The concentrations in the storage-dominated regimes M and K are larger than in the leak-off-dominated regimes $\widetilde{M}$ and $\widetilde{K}$ for both the fracture tip and body, which shows that the leak-off leads to a reduction in the concentration.

(3) Poroelastic effects P_c/P_p and σ_b/P_p are slightly affected by fracturing regimes at the fracture tip but strongly affected by fracturing regimes in the fracture body. Their effect will induce a prominent peak shifting between confining stress response and pore pressure in the viscosity-dominated regimes.

(4) The constitutive relationships between the confining stress response and hydraulic volumetric opening are strongly governed by hydraulic fracturing regimes. The time span of the peak confining stress response is shorter in the M regime than in the other three limiting regimes.

Author Contributions: Formal analysis, funding acquisition, methodology, supervision, writing—review and editing, S.G.; data analysis, writing—review, Y.C.; conceptualization, writing—original and editing, L.W. and H.L.; review and editing, X.Z. and W.Z.; data analysis, Z.C. and B.M. All authors have read and agreed to the published version of the manuscript.

Funding: This work was supported by the National Natural Science Foundation of China (grant No. 42230814, grant No. 12272126, and grant No. 52004082).

Data Availability Statement: Data were curated by the authors and are available upon request.

Conflicts of Interest: The authors declare no conflict of interest.

References

1. Tian, L.; Cao, Y.; Chai, X.; Liu, T.; Feng, P.; Feng, H.; Zhou, D.; Shi, B.; Oestreich, R.; Rodvelt, G. Best practices for the determination of low-pressure/permeability coalbed methane reservoirs, Yuwu Coal Mine, Luan mining area, China. *Fuel* **2015**, *160*, 100–107. [CrossRef]
2. Mou, P.; Pan, J.; Wang, K.; Wei, J.; Yang, Y.; Wang, X. Influences of hydraulic fracturing on microfractures of high-rank coal under different in-situ stress conditions. *Fuel* **2021**, *287*, 119566. [CrossRef]
3. Xu, S.; Guo, J.; Feng, Q.; Ren, G.; Li, Y.; Wang, S. Optimization of hydraulic fracturing treatment parameters to maximize economic benefit in tight oil. *Fuel* **2022**, *329*, 125329. [CrossRef]
4. Lin, B.; Meng, H.; Pan, J.; Chen, S. Porothermoelastic response of an oil sand formation subjected to injection and micro-fracturing in horizontal wells. *Petrol. Sci.* **2020**, *17*, 687–700. [CrossRef]
5. Wang, L.; Xue, Y.; Cao, Z.; Kong, H.; Han, J.; Zhang, Z. Experimental Study on Mode I Fracture Characteristics of Granite after Low Temperature Cooling with Liquid Nitrogen. *Water* **2023**, *15*, 3442. [CrossRef]
6. Zhang, X.; Cao, Y.; Wang, L.; Xiaohui, G. Poromechanical Modeling and Numerical Simulation of Hydraulic Fracture Propagation. *ACS Omega* **2022**, *7*, 25003–25012. [CrossRef] [PubMed]
7. Zhang, F.; Huang, L.; Yang, L.; Dontsov, E.; Weng, D.; Liang, H.; Yin, Z.; Tang, J. Numerical investigation on the effect of depletion-induced stress reorientation on infill well hydraulic fracture propagation. *Petrol. Sci.* **2022**, *19*, 296–308. [CrossRef]
8. Zhang, Z.; Zhang, R.; Wu, S.; Deng, J.; Zhang, Z.; Xie, J. The Stress Sensitivity and Porosity Sensitivity of Coal Permeability at Different Depths: A Case Study in the Pingdingshan Mining Area. *Rock Mech. Rock Eng.* **2019**, *52*, 1539–1563. [CrossRef]
9. Wasantha, P.L.P.; Konietzky, H.; Xu, C. Effect of in-situ stress contrast on fracture containment during single- and multi-stage hydraulic fracturing. *Eng. Fract. Mech.* **2019**, *205*, 175–189. [CrossRef]
10. Zhao, X.; Huang, B. Distribution Relationship of Pore Pressure and Matrix Stress during Hydraulic Fracturing. *ACS Omega* **2021**, *6*, 30569–30579. [CrossRef]
11. Zhao, W.; Wang, K.; Wang, L.; Cheng, Y.; Dong, H.; Li, B.; Dai, L. Influence of matrix size and pore damage path on the size dependence of gas adsorption capacity of coal. *Fuel* **2021**, *283*, 119289. [CrossRef]
12. Haenel, M.W. Recent progress in coal structure research. *Fuel* **1992**, *71*, 1211–1223. [CrossRef]
13. Cleary, M.P. Analysis of Mechanisms and Procedures for Producing Favourable Shapes of Hydraulic Fractures. In Proceedings of the SPE Annual Technical Conference and Exhibition, Dallas, TX, USA, 21 September 1980.
14. Detournay, E.; Cheng, A.; Roegiers, J.C.; McLennan, J.D. Poroelasticity considerations in in situ stress determination by hydraulic fracturing. *Int. J. Rock Mech. Min.* **1989**, *26*, 507–513. [CrossRef]
15. Detournay, E.; Cheng, A.; McLennan, J.D. A Poroelastic PKN Hydraulic Fracture Model Based on an Explicit Moving Mesh Algorithm. *J. Energy Resour.-Asme* **1990**, *112*, 224–230. [CrossRef]
16. Kovalyshen, Y. Fluid-Driven Fracture in Poroelastic Medium. Ph.D. Thesis, The University of Minnesota, Minneapolis, MN, USA, 2010.
17. Boone, T.J.; Ingraffea, A.R.; Roegiers, J.C. Simulation of hydraulic fracture propagation in poroelastic rock with application to stress measurement techniques. *Int. J. Rock Mech. Min. Sci. Geomech. Abstr.* **1991**, *28*, 1–14. [CrossRef]
18. Golovin, S.V.; Baykin, A.N. Influence of pore pressure on the development of a hydraulic fracture in poroelastic medium. *Int. J. Rock Mech. Min.* **2018**, *108*, 198–208. [CrossRef]
19. Gao, Y.; Detournay, E. A poroelastic model for laboratory hydraulic fracturing of weak permeable rock. *J. Mech. Phys. Solids* **2020**, *143*, 104090. [CrossRef]
20. Baykin, A.N. The range of influence of the poroelastic effects in terms of dimensionless complexes for the radial hydraulic fracturing model. *Int. J. Rock Mech. Min.* **2020**, *128*, 104240. [CrossRef]
21. Dontsov, E.V. An efficient computation of leak-off induced poroelastic stress for a hydraulic fracture. *J. Mech. Phys. Solids* **2021**, *147*, 104246. [CrossRef]
22. Sarris, E.; Papanastasiou, P. The influence of the cohesive process zone in hydraulic fracturing modelling. *Int. J. Fract.* **2011**, *167*, 33–45. [CrossRef]
23. Sarris, E.; Papanastasiou, P. Numerical modeling of fluid-driven fractures in cohesive poroelastoplastic continuum. *Int. J. Numer. Anal. Methods* **2013**, *37*, 1822–1846. [CrossRef]
24. Sarris, E.N.; Papanastasiou, P. The influence of pumping parameters in fluid-driven fractures in weak porous formations. *Int. J. Numer. Anal. Methods* **2015**, *39*, 635–654. [CrossRef]
25. Yoon, J.S.; Zimmermann, G.; Zang, A. Numerical Investigation on Stress Shadowing in Fluid Injection-Induced Fracture Propagation in Naturally Fractured Geothermal Reservoirs. *Rock Mech. Rock Eng.* **2015**, *48*, 1439–1454. [CrossRef]
26. Han, W.; Cui, Z.; Zhang, J. Fracture path interaction of two adjacent perforations subjected to different injection rate increments. *Comput. Geotech.* **2020**, *122*, 103500. [CrossRef]
27. Wang, H. Poro-elasto-plastic modeling of complex hydraulic fracture propagation: Simultaneous multi-fracturing and producing well interference. *Acta Mech.* **2016**, *227*, 507–525. [CrossRef]
28. Taghichian, A.; Hashemalhoseini, H.; Zaman, M.; Yang, Z. Geomechanical optimization of hydraulic fracturing in unconventional reservoirs: A semi-analytical approach. *Int. J. Fract.* **2018**, *213*, 107–138. [CrossRef]

29. Ma, G.; Wang, Y.; Li, T.; Chen, Y. A mesh mapping method for simulating stress-dependent permeability of three-dimensional discrete fracture networks in rocks. *Comput. Geotech.* **2019**, *108*, 95–106. [CrossRef]
30. Wangen, M. A 3D model of hydraulic fracturing and microseismicity in anisotropic stress fields. *Geomech. Geophys. Geo* **2019**, *5*, 17–35. [CrossRef]
31. Lee, S.; Min, B.; Wheeler, M.F. Optimal design of hydraulic fracturing in porous media using the phase field fracture model coupled with genetic algorithm. *Computat. Geosci.* **2018**, *22*, 833–849. [CrossRef]
32. Liu, X.; Rasouli, V.; Guo, T.; Qu, Z.; Sun, Y.; Damjanac, B. Numerical simulation of stress shadow in multiple cluster hydraulic fracturing in horizontal wells based on lattice modelling. *Eng. Fract. Mech.* **2020**, *238*, 107278. [CrossRef]
33. Dontsov, E.V.; Suarez-Rivera, R. Propagation of multiple hydraulic fractures in different regimes. *Int. J. Rock Mech. Min.* **2020**, *128*, 104270. [CrossRef]
34. Wang, L.; Xu, H.; Cao, Y.; Liu, S. A poromechanical model of hydraulic fracturing volumetric opening. *Eng. Fract. Mech.* **2020**, *235*, 107172. [CrossRef]
35. Zimmerman, R.W. Coupling in poroelasticity and thermoelasticity. *Int J Rock Mech Min* **2000**, *37*, 79–87. [CrossRef]
36. Barenblatt, G.I. The Mathematical Theory of Equilibrium Cracks in Brittle Fracture. *Adv. Appl. Mech.* **1962**, *7*, 55–129.
37. Garagash, D.I.; Detournay, E. Plane-Strain Propagation of a Fluid-Driven Fracture: Small Toughness Solution. *J. Appl. Mech.* **2005**, *72*, 916–928. [CrossRef]
38. Bunger, A.P.; Detournay, E.; Garagash, D.I. Toughness-dominated Hydraulic Fracture with Leak-off. *Int. J. Fract.* **2005**, *134*, 175–190. [CrossRef]
39. Adachi, J.I.; Detournay, E. Plane strain propagation of a hydraulic fracture in a permeable rock. *Eng. Fract. Mech.* **2008**, *75*, 4666–4694. [CrossRef]
40. Hu, J.; Garagash, D.I. Plane-Strain Propagation of a Fluid-Driven Crack in a Permeable Rock with Fracture Toughness. *J. Eng. Mech.-Asce* **2010**, *136*, 1152–1166. [CrossRef]